ADVANCED OPTICAL MATERIALS
www.advopticalmat.de

Blue-Emitting Boron- and Nitrogen-Doped Carbon Dots for White Light-Emitting Electrochemical Cells

Luca M. Cavinato, Veronika Kost, Sergi Campos-Jara, Sara Ferrara, Sanchari Chowdhury, Irene M.N. Groot, Tatiana Da Ros,* and Rubén D. Costa**

This work describes the first use of blue-emitting boron- and nitrogen-doped carbon dots (BN-CDs), rationalizing their photoluminescence behavior in solution and ion-based thin-films to prepare white light-emitting electrochemical cells (LECs). In detail, a cost-effective and scalable water-based microwave-assisted synthesis procedure is set for BN-CDs featuring an amorphous carbon-core doped with N and B. While they show a bright (photoluminescence quantum yield of 42%) and excitation-independent blue-emission (440 nm) in solution related to emitting n−π^* surface states, they are not emissive in thin-films due to aggregation-induced quenching. Upon fine-tuning the film composition (ion-based host), an excitation dependent emission covering the whole visible range is noted caused by interaction of the ion electrolyte with the peripheral functionalization of the BN-CDs. Moreover, the efficient energy transfer from the host to the BN-CDs emitting species enabled good performing LECs with white emission (*x*/*y* CIE coordinates of 0.30/0.35, correlated color temperature of 6795 K, color rendering index of 87) and maximum luminance of 40 cd m^{-2}, and stabilities of a few hours. This represents a significant improvement compared to the prior-art monochromatic CD-based LECs with similar brightness levels, but stabilities of <1 min.

1. Introduction

Light-emitting electrochemical cells (LECs) are single-layered electroluminescent devices, offering a moderate lighting performance at low-cost production.[1] Their simple architecture relies on the presence of mobile ions in the active layer (i.e., emitter: electrolyte blend). Upon biasing the device, the ions redistribution toward the electrode interface assists the electrochemical doping, forming a *p-i–n* junction structure.[2] This operational mode leads to a high tolerance toward *i*) the working function of the electrodes allowing the use of air-stable materials,[3] and *ii*) large thickness and roughness tolerance of the active layer.[4] These features enable the fabrication of LECs using cheap and upscalable solution-based techniques on arbitrary electrodes and 3D shapes as well as the use of a huge palette of emitters (i.e., conjugated polymers, ionic transition metal complexes, small molecules, dendrimers, and perovskites).[5–11] Finally, LECs are recently evolving toward fulfilling sustainability goals as reusable or disposable lighting devices. A leading example is the integration of sustainable and/or biogenic emitters and electrolytes.[12] In this context, carbon dots (CDs) are promising emitters for thin-film lighting devices[13–17] due to their tunable photo-/electroluminescent (PL/EL) properties, non-toxicity, and relatively easy, green, large-scale production.[18] Particularly, microwave-assisted "bottom-up" preparation methods allow synthesis from widely available, cheap, and non-hazardous small organic molecules and polymers through mild and fast treatments in water media solutions.[19–24] Finally, the variety of precursors provides a unique opportunity to fine tune structure and surface composition, influencing both PL/EL properties.[25]

Though carbon-based CDs are of high interest for thin-film lighting, the major roadblock is their effective incorporation in the active layer due to *i*) poor compatibility with standard hole/electron transport layers and host materials in organic solvents for solvent-based deposition techniques upon device fabrication, and *ii*) prominent phase separation and aggregation-induced emission quenching in thin films.[26,27] Recently, efforts have successfully circumvented them via *i*) surface modification approach,[28] *ii*) functionalization with polyvinyl

L. M. Cavinato, S. Ferrara, S. Chowdhury, R. D. Costa
Technical University of Munich, Chair of Biogenic Functional Materials
Campus Straubing for Biotechnology and Sustainable
Schulgasse 22, 94315 Straubing, Germany
E-mail: ruben.costa@tum.de

V. Kost, T. Da Ros
Department of Chemical and Pharmaceutical Sciences
University of Trieste
Via Giorgieri 1, Trieste 34127, Italy
E-mail: daros@units.it

S. Campos-Jara, I. M. Groot
Leiden Institute of Chemistry
Leiden University
P.O. Box 9502, Leiden 2300 RA, The Netherlands
E-mail: i.m.n.groot@lic.leidenuniv.nl

The ORCID identification number(s) for the author(s) of this article can be found under https://doi.org/10.1002/adom.202400618

© 2024 The Author(s). Advanced Optical Materials published by Wiley-VCH GmbH. This is an open access article under the terms of the Creative Commons Attribution-NonCommercial License, which permits use, distribution and reproduction in any medium, provided the original work is properly cited and is not used for commercial purposes.

DOI: 10.1002/adom.202400618

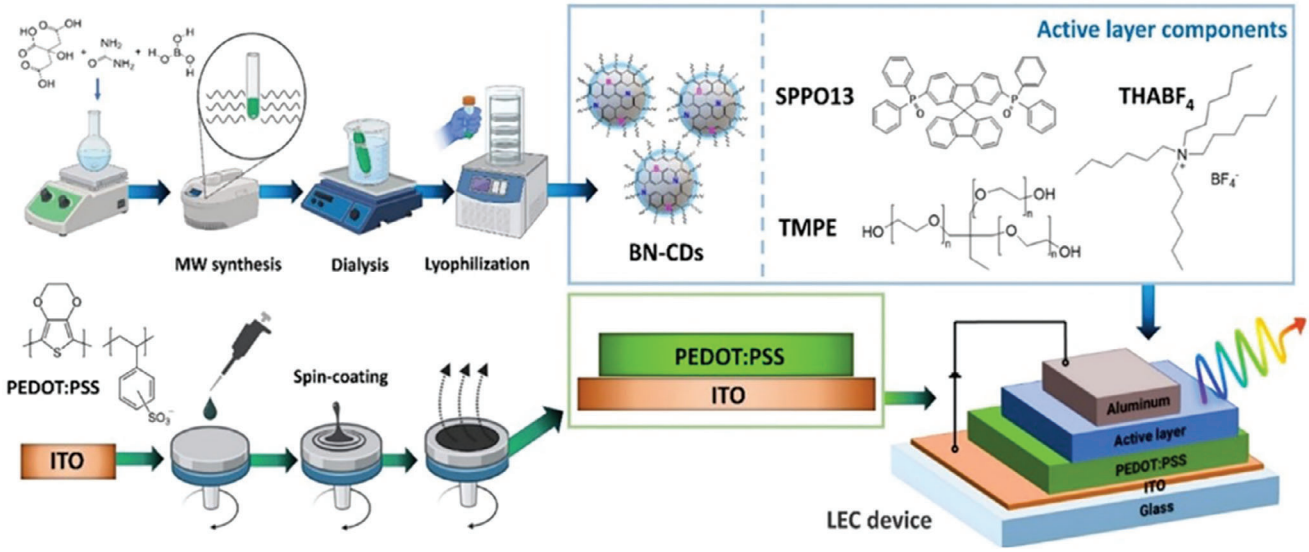

Figure 1. Scheme of synthesis of BN-CDs and integration to prepare white LECs.

alcohol (PVA),[29] *iii)* incorporation of CDs in a hydrophilic-solid matrix,[15,17] and *iv)* incorporation of CDs in micelles.[27] Yet, a fabrication method that relies on green solvents has not been achieved, reaching moderate device performances. For instance, a handful number of reports in monochromatic (blue- and red-emitting) CDs-LECs presented moderate performances with device stabilities <1 min and brightness of ≈80–100 cd m^{-2}.[15,17,27]

Herein, we demonstrate two new concepts with respect to material design and device fabrication at force to advance CDs-based LECs, realizing the first white-emitting device. At first, we disclose a quick and simple water-based microwave-assisted method to prepare boron and nitrogen doped CDs using cheap and commercially available precursors, such as citric acid (CA), boric acid (BA), and urea (U) (**Figure 1**). In contrast to heteroatom-free CDs, the N-doping results in improved PL quantum yields (PLQYs),[27] while the B-doping leads to enhanced stabilities toward photobleaching and chemical stress.[30,31] The BN-CDs feature excitation-independent narrow blue emission (peak wavelength = 440 nm, full width at half maximum (FWHM) = 60 nm) with a high PLQY of 42% in diluted aqueous solution. In contrast, thin-films exhibited a lack of emission as they are prone to aggregate. This was circumvented using a hydrophilic host matrix based on amorphous 2,7-bis(diphenylphosphoryl)−9,9′-spirobifluorene (SPPO13) and a mixture of tetrahexylammonium tetrafluoroborate ($THABF_4$) and trimethylolpropane ethoxylate (TMPE) as ion electrolyte (Figure 1). These homogenous thin-films exhibited *i)* an excitation-dependent emission covering the whole visible range due to the interaction of the ions with the emitting n−π^* surface states, and *ii)* an efficient energy transfer from the host to the BN-CDs. This resulted in a peculiar EL behavior in LECs with a white-emission (*x/y Commission Internationale de l'Eclairage* (CIE) coordinates of 0.30/0.35, color correlated temperature (CCT) of 6795 K, and color rendering index (CRI) of 87) associated to maximum luminance of 40 cd m^{-2} and significantly improved stability in the range of hours compared to prior-art (<1 min) – Table S1 (Supporting Information).[15,17,27]

Overall, this work demonstrates *i)* an easy up-scalable way to produce highly luminescent and stable BN-CDs and *ii)* how to easily integrate them in good performing LECs using environmentally friendly solution-processed techniques, toward eco-friendly white-emitting lighting systems.

2. Results and Discussion

2.1. Synthesis and Characterization of BN-CDs

The bottom-up microwave synthesis of BN-CDs was performed using a mixture of CA, BA, and U as carbon, boron, and nitrogen sources, respectively. The precursors were chosen due to their low toxicity, wide availability, and high solubility in water. The thermal treatment of the precursors and the following purification by dialysis were performed using water that stands out from other solvents by its negligible environmental impact. The water-based production approach was beneficial for environment and allowed the production of BN- nanodots with high PLQY.[33] However, for carbon dots derived from CA and various amines/amides, the origin of superior PL properties is subject to debate, since the production process can lead to the presence of molecular fluorophores, which might be responsible for, or at least contribute to, fluorescence.[32–34] In the case of dual doping with B and N, the contribution of molecular species to the PL behavior of BN-CDs was indicated for those derived from aromatic precursors.[35] Indeed, the research work on BN-CDs from aliphatic sources[32,36] has been mainly focused on the microscopic characterization of the final product using transmission electron microscopy (TEM) and atomic force microscopy (AFM) techniques suitable for nanomaterials. Thus, this lacks the spectroscopic characterization necessary to confirm the presence or absence of fluorescent molecular species. To tackle this problem, we controlled the purification of BN-CDs by UV–vis, PL, and ^{1}H-NMR spectroscopy.

It is common knowledge that the synthesis temperature plays a crucial role in the formation of nanoparticles, affecting the

© 2024 The Author(s). Advanced Optical Materials published by Wiley-VCH GmbH

21951071, 2024, 27, Downloaded from https://advanced.onlinelibrary.wiley.com/doi/10.1002/adom.202400618 by Universita Di Torino, Wiley Online Library on [13/03/2025]. See the Terms and Conditions (https://onlinelibrary.wiley.com/terms-and-conditions) on Wiley Online Library for rules of use; OA articles are governed by the applicable Creative Commons License

formation of side products, including molecular fluorophores.[33,37] In the case of citric acid/urea-based microwave synthesis, temperatures above 150 °C were found to promote the reactivity of the precursor mixture, while performing the reaction at 180 °C allowed the consumption of CA and U with a drastic increase in its yield.[33] Therefore, we performed reactions with CA, BA, and U (1:1:1 in mass) between 160–190 °C, using steps of 10 °C. The as-obtained samples showed bright blue PL before dialysis; however, the following purification led to a significant loss in PLQY values for those prepared at T≤ 180 °C, as shown in Table S2 (Supporting Information). The UV–vis and FL measurements of the dialysis water collected after 2 h of purification (Table S3, Supporting Information) showed light absorption and emission behavior similar to those observed before dialysis. At the same time, the dialyzed samples deriving from syntheses performed at T≤ 180 °C were obtained with very low reaction yield (<1%), as presented in Table S2 (Supporting Information). Considering these findings, we could assume that the fluorescent species in the dialysis water were mostly part of molecular side-products eliminated by purification.

In contrast, the synthesis at 190 °C allowed a high reaction yield (20%) with a slight change in the PL properties after the purification step. Performing the reaction at 190 °C but in the absence of boric acid (mass ratio of CA:BA:U 1:0:1) resulted in both low reaction and quantum yields (Table S4, Supporting Information). Further increasing the amount of boric acid or urea in the mixture of CA, BA, U to 1:3:1 and 1:1:3, respectively, allowed an improvement in PL properties and achieved higher reaction yield (Table S4, Supporting Information), however, still not reaching the values of 1:1:1 CA:BA:U sample. Therefore, the MW conditions of 190 °C and 1:1:1 starting materials' ratio were optimal in terms of both reaction yield and PL properties, and this BN-CDs sample was chosen for the further application, and so properly characterized.

The microscopic analyses of BN-CDs (190 °C, CA:BA:U 1:1:1) proved the formation of uniformly distributed disc-shaped nanoparticles with an average size of 4.02 ± 1.22 nm and height of 2.42 ± 0.66 nm, according to TEM and AFM results, respectively (**Figure 2**).

Taking into consideration that AFM images of spherical molecular aggregates might resemble those of nanoparticles,[38] we complemented the microscopic analyses with ^{1}H-NMR spectroscopy to determine the possible presence of co-formed molecular fluorophores in the purified materials. Among the potential molecular products deriving from citric acid and urea-based synthesis, citrazinic acid (CTA) and 4-hydroxy-1H-pyrrolo[3,4-c]pyridine-1,3,6(2H,5H)-trione (HPPT) stand out by the bright blue and green fluorescence, respectively. The chosen reaction conditions allow us to assume that the formation of CTA could be more favorable since the BN-CDs synthesis was performed in water, preventing the CTA from further reaction with isocyanic acid toward the formation of HPPT.[34] Hence, in principle CTA might be detected in the reaction mixture, with a possibility of observing traces of HPPT as well. The ^{1}H-NMR spectrum of purified BN-CDs (Figure S1, Supporting Information) did not present intense sharp peaks, commonly associated with molecular species. The low-intensity signals detected at 2.8–2.6 ppm range (Figure S1a, Supporting Information) are attributed to traces of citric acid, and those at ≈7.1 ppm to residual ammonium salts in the product mixture, while the urea characteristic signal at 5.4 ppm (Figure S1b, Supporting Information) is not present. Considering the non-fluorescent nature of the molecular traces observed, it is reasonable to assume that they cannot contribute to the PL properties of the BN-CDs sample. A further comparative analysis was performed taking into consideration the ^{1}H-NMR of CTA: the signal at 6.2 ppm, characteristic of the two aromatic protons of CTA, was not present in the BN-CDs spectrum (Figure S1c, Supporting Information), as well as the broad signal at 12 ppm, corresponding to the carboxylic acid proton. These evidences corroborate our statement about the absence of CTA in the BN-CDs sample. Eventually, also the ^{1}H-NMR spectrum of HPPT from literature[34] was compared with the BN-CDs one, without finding any common peaks, being the fluorophore ones at 9.9 and 5.4 ppm. Thus, the ^{1}H-NMR analysis conducted for the BN-CDs sample confirms the purity of the nanomaterial and its intrinsic fluorescent nature.

Next, the structural features of BN-CDs were investigated by FTIR, Raman spectroscopy and XRD analysis. The Raman spectrum (Figure S2, Supporting Information) shows two peaks at 1325 and 1588 cm^{-1} for the D and G band, respectively, corresponding to amorphous/defective carbon and crystalline sp^2-domains.[28,39] The doping of the carbon core with B and N introduced the defects to the structure, leading to the broadening and shifting of the D and G band.[39] The intensity ratio of I_D/I_G was calculated as 1.06, indicating the predominance of disordered (amorphous) carbon structures for the nanoparticles.[39] Characteristic for graphene 2D peak that can indicate that the number of layers of graphene was not well-defined, which can be associated with either an amorphous structure of carbon core or a small size (4 nm) of synthesized BN-CDs, since with increasing in nanoparticles' diameter, the higher-order mode is observed as a more prominent intense peak.[39] The following XRD analysis (Figure S3, Supporting Information) did not succeed in identifying definitive characteristic signals apart from those found in the substrate, possibly due to the nanomaterial's amorphous nature. It is worth noting that the UV–vis spectrum of BN-CDs in aqueous solution reveals absorption bands centered at 235 and 340 nm, which are attributed to π–π^* and n–π^* surface state transitions, respectively (Figure S4, Supporting Information). This is in contrast to the typical absorption band of undoped carbon dots with the crystalline core.[28]

The presence of dopants in the BN-CDs carbon core and surface was further confirmed by ATR-FTIR analysis. As depicted in **Figure 3**, the FTIR spectra of BN-CDs revealed broad peaks in the range of 3000–3500 cm^{-1}, which are associated with the hydroxyl and amino groups on the surface of BN-CDs. Additionally, the stretching vibrations observed at 1718, 1679, and 1560 cm^{-1} are indicative of the bonding of C═O/C═N and C—N, respectively, and could be attributed to the presence of carboxylic acid groups and nitrogen-containing moieties on the surface. Together with the B—OH stretching vibration observed at 1247 cm^{-1}, we can assume that good water solubility of synthesized nanoparticles arises from various polar functional groups on the surface of BN-CDs.[40] The peaks centered at 1103 and 1072 cm^{-1} confirmed the bonding of boron to carbon (B—C) and oxygen (B—O—C), respectively.[41,42]The stretching vibration of B-N are represented by a peak observed at 1419 cm^{-1}, along with several peaks in

© 2024 The Author(s). Advanced Optical Materials published by Wiley-VCH GmbH

21951071, 2024, 27, Downloaded from https://advanced.onlinelibrary.wiley.com/doi/10.1002/adom.202400618 by Universita Di Torino, Wiley Online Library on [13/03/2025]. See the Terms and Conditions (https://onlinelibrary.wiley.com/terms-and-conditions) on Wiley Online Library for rules of use; OA articles are governed by the applicable Creative Commons License

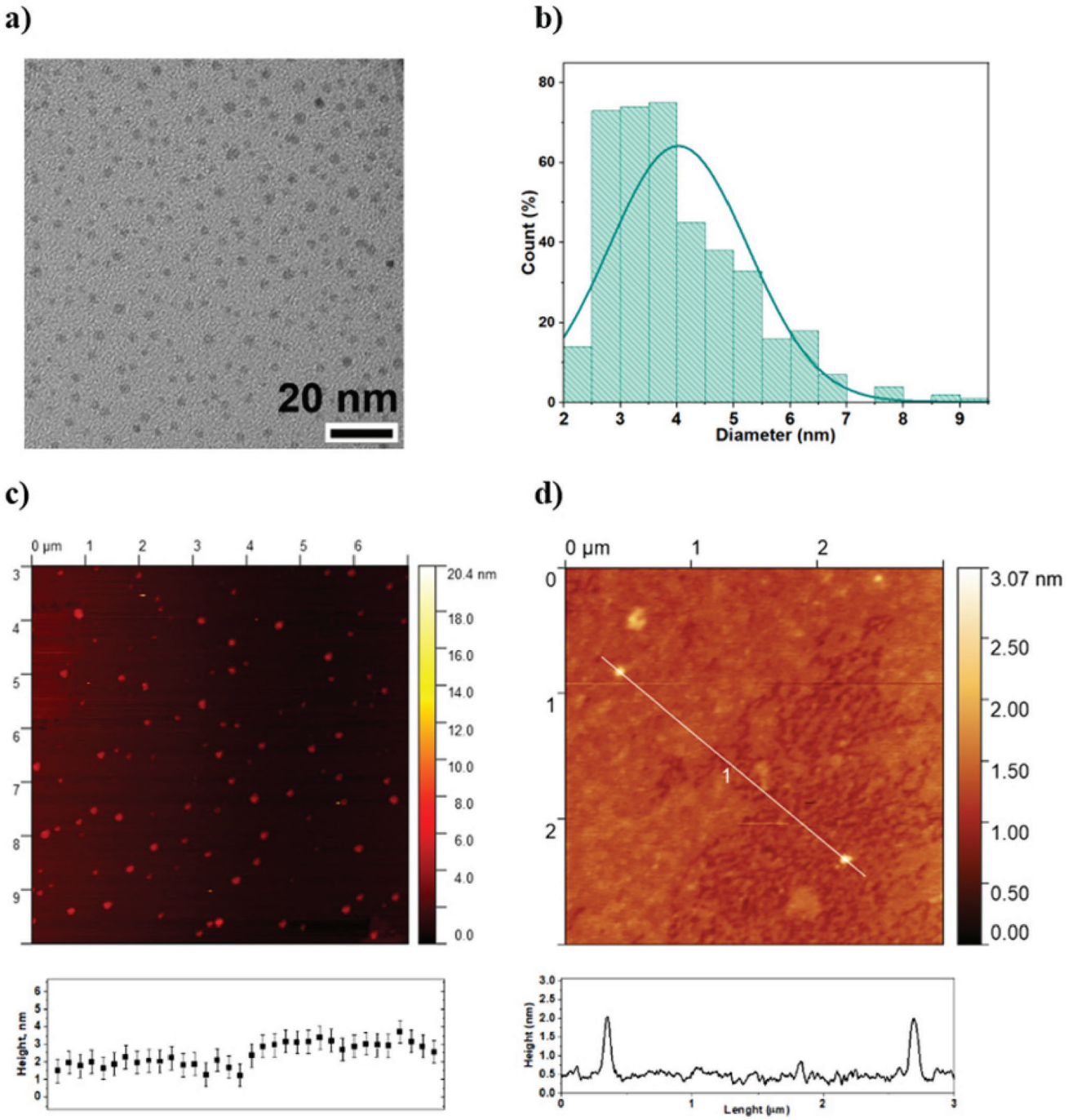

Figure 2. a) TEM image of BN-CDs and b) corresponding particle size distribution diagram. AFM images of BN-CDs of c) 70 μm^2 area with error bar and d) 3 μm^2 area with corresponding height profile.

the range of 669–890 cm^{-1}, while the peaks at 943 and 974 cm^{-1} are assigned to N—B—O bonding.[36,42] Due to the similarity of the functional groups on the surface of BN-CDs (-OH, -COOH,-NH_2,-B-OH) with those for starting materials, the signals were observed in the same areas.[36] However, the BN-CDs' peaks appear broader and shifted than those for CA, BA, and U (Figure S5, Supporting Information), indicating the difference between molecular precursors and nanoparticles.

Finally, X-ray photoelectron spectroscopy (XPS) confirmed the presence of boron and nitrogen doping in the form of B—N, B—C, and N—C bonds with an overall atomic distribution consisting of C, O, N, and B atomic percentages of 18, 77, 5.1, and 0.14%, respectively (**Figure** 4a–d). The high-resolution XPS spectrum can be deconvoluted for each element as follows: *i*) the C1s spectrum (Figure 4b) displays five peaks at 291.0, 289.5, 287.5, 284.9, and 284.0 eV that correspond to C=O, C—O, C—N, C—C/C—H, and

© 2024 The Author(s). Advanced Optical Materials published by Wiley-VCH GmbH

21951071, 2024, 27, Downloaded from https://advanced.onlinelibrary.wiley.com/doi/10.1002/adom.202400618 by Universita Di Torino, Wiley Online Library on [13/03/2025]. See the Terms and Conditions (https://onlinelibrary.wiley.com/terms-and-conditions) on Wiley Online Library for rules of use; OA articles are governed by the applicable Creative Commons License

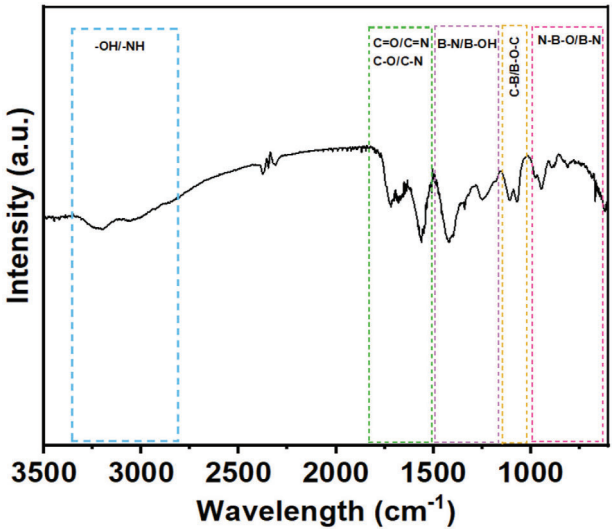

Figure 3. ATR-FTIR spectrum of BN-CDs.

C—B bonds, respectively, *ii*) the N1s spectrum (Figure 4c) shows 4 peaks, located at 403.8, 402.0, 400.5, and 397.5 eV, corresponding to NO_x, N graphitic, N pyrrolic, and N-B, *iii*) the B1s spectrum (Figure 4d) features 3 components corresponding to B-C_2-O, B-N, B-C, and B-O at 195.3, 194.2, 192.8, and 190.5 eV,[40,43–46] respectively, and *iv*) the O1s spectrum (Figure S6, Supporting Information) was deconvoluted into 4 peaks at 532.0, 533.0, 534.1, and 534.2 eV attributed to O—H, C—O, C═O, and B—O bonds, respectively.

As expected, the difference in concentration of the different elements is in good correlation with the way the synthesis is performed and the concentration of the elements in the different precursors. The concentration of the elements (O, C, N and B) within the three precursors is 52.3%, 33.3%, 9.50% and 4.70%, respectively. It is worth noting that the BN-CDs synthesis was performed in water, starting from oxygen-rich precursors. Moreover, it should be considered that the formation of a C—C and a C—N bond is chemically much more favorable than a C—B and B—N bond. Besides, the B can oxidize easily and leave in gaseous form. In addition, B has a lower XPS cross section than C, N, and O. All these factors together explain the lower peak intensity detected in the XPS survey in Figure 4a. The higher presence of carbon and oxygen explains why, despite the high intensity of the B—C and B—N contributions in the B1s core level in Figure 4d, when observing the C1s and N1s core levels in Figure 3b,c, respectively, C—B and N—B contributions are so small. This can also be observed for the C—N contribution in the C1s core level shown in Figure 4b. Because of their higher concentration, C and O have a much higher intensity compared to Figure 4c where the intensity of the N—C bond in graphitic and pyrrolic form is higher.

2.2. Photoluminescent Behavior of BN-CDs

Upon excitation at 350 nm, the BN-CDs showed a structureless emission band centered at ≈440 nm in diluted (<1 mg mL^{-1}) milliQ aqueous solutions, while the excitation spectra mainly consist of a broad peak at 350 nm (**Figure 5a**). The intense blue emission of BN-CDs aqueous solutions is associated to a mono-exponential excited state lifetime (τ) of 6.77 ns and a PLQY of 42%. In contrast with the prior-art all carbon-based CDs,[47,48] BN-CDs exhibited an excitation-wavelength independent PL response (Figure 5b) that suggests a localized excited n−π^* surface state and homogeneous nanosize distribution (vide supra). However, the gradual increase of the concentration up to 20 mg mL^{-1} leads to a small (<10 nm) red-shift of the emission band and a reduction of the PLQY down to 17% (Figure 5c). Noteworthy, at high concentration the emission is not anymore excitation-independent (Figure 5d); more in detail, up to excitation wavelengths of 395 nm the maximum of the emission is preserved at ≈460 nm while at longer excitation wavelengths the emission is greatly red-shifted, reaching emission maximum at 540 nm upon excitation at 440 nm (Figure S7, Supporting Information). Since the UV–vis absorption spectra is not affected by the BN-CDs concentration (Figure S7, Supporting Information), the PL changes must be attributed to the presence of poor emissive excimer-like species caused by aggregation.[49,50]

At this point, we prepared neat BN-CDs films via spin-coating. To the naked eye, the morphology of the films consists of large aggregates that are not emissive under UV-lamp excitation with a PLQY that is nearly zero (Figure 5c). Thus, we decided to focus on a host–guest strategy using the amphiphilic host SPPO13 and a mixture of $THABF_4$ and TMPE as the ions source. The criterion of materials selection is based on previous literature and optimization.[15,17] $THABF_4$ has recently shown a good compatibility with CNDs in hydrophilic solvents, enabling the preparation of emissive and homogeneous films.[15,17] In addition, there is a desired spectral overlap between the emission spectrum of the SPPO13-based host matrix and the excitation spectrum of the diluted BN-CDs' aqueous solution (Figure S8, Supporting Information), allowing an efficient energy transfer from the host to the BN-CDs guest (vide infra).[51] Finally, the presence of TMPE is important to ensure sub-nanometric root mean square (RMS) roughness (Figure S9, Supporting Information), which is vital for the correct working mechanism of devices. In fact, both thin-films with composition SPPO13:$THABF_4$:BN-CDs:TMPE 1:0.2:0.6:0.2 and 1:0.2:0.0:0.2 (prepared for reference purposes) showed a homogeneous morphology, as confirmed by AFM mapping. In contrast, thin films with composition 1:0.2:0.6:0.0 show high value of RMS (i.e., 4208 pm), rendering them incompatible for device fabrication. In terms of PL features, SPPO13:$THABF_4$ based films exhibit a sharp peak in the UV region upon excitation (λ_{exc} = 300 nm), with a full width at half maximum (FWHM) of less than 50 nm, specifically centered at 365 nm. This peak is associated with a PLQY of 13% and an excited-state lifetime of 4.15 ns. Importantly, the PL response remains unchanged upon addition of TMPE – see **Table 1**. Upon addition of BN-CDs to the blend, a dual PL response was recorded under excitation at 300 nm. The two emission bands are centered at 330 nm and 440 nm, corresponding to the residual emission of the host matrix and that of the BN-CDs, respectively (Figure S10, Supporting Information). Furthermore, there is a significant decrease of the τ values of the host emission from 5.0 to 1.69 ns upon adding BN-CDs, while the PLQY of the films holds constant at ≈15%. Quantitative evaluation of the energy transfer efficiency

© 2024 The Author(s). Advanced Optical Materials published by Wiley-VCH GmbH

21951071, 2024, 27, Downloaded from https://advanced.onlinelibrary.wiley.com/doi/10.1002/adom.202400618 by Universita Di Torino, Wiley Online Library on [13/03/2025]. See the Terms and Conditions (https://onlinelibrary.wiley.com/terms-and-conditions) on Wiley Online Library for rules of use; OA articles are governed by the applicable Creative Commons License

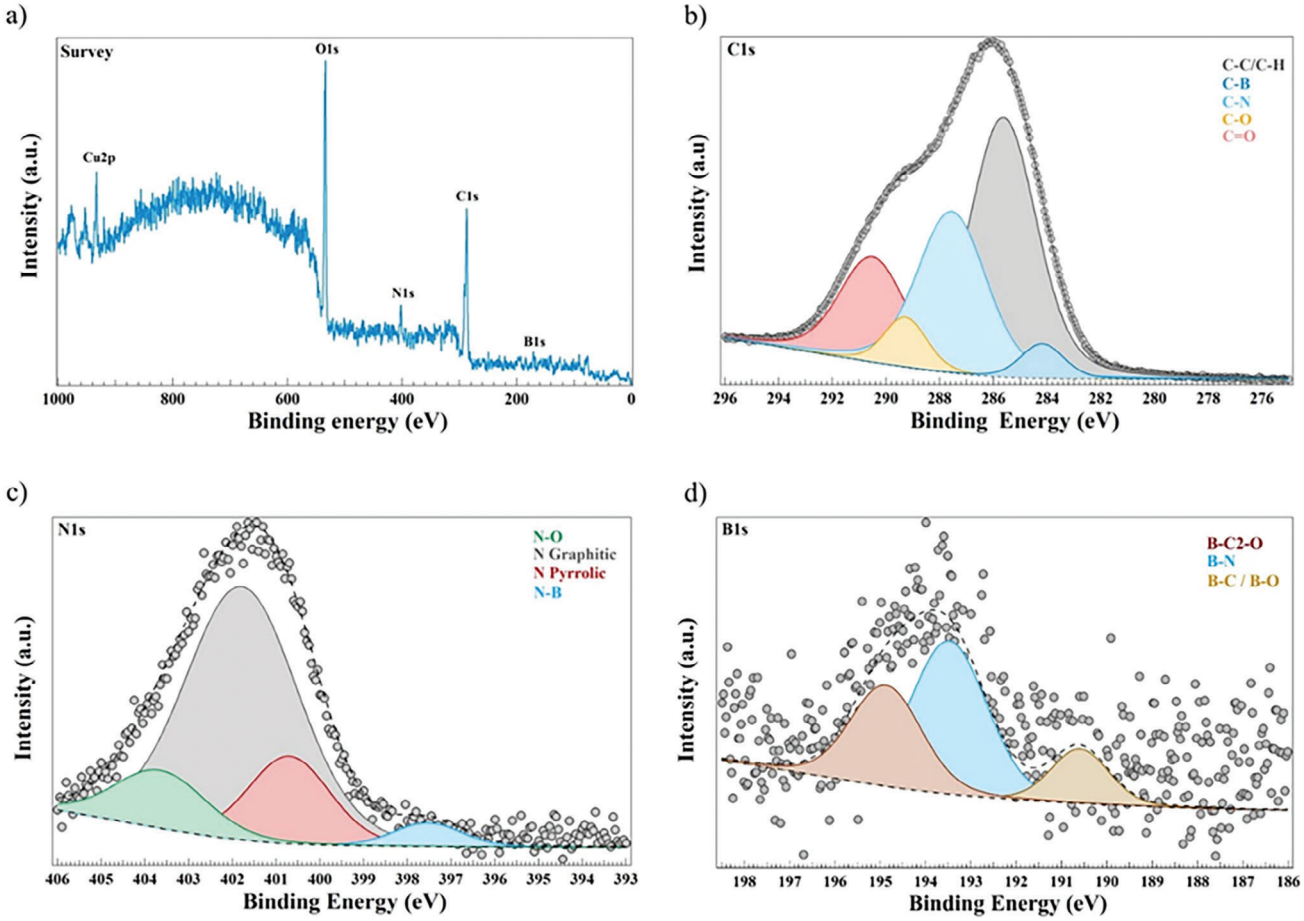

Figure 4. XPS characterization of the BN-CDs. a) Survey spectrum of BN-CDs adsorbed onto a copper substrate; b) C1s core level spectrum; c) N1s core level spectrum; d) B1s core level spectrum.

(γ_{ET}) of the obtained luminescent films was performed following Equation 1:[52]

$$\gamma_{ET} = 1 - \frac{I_{DA}}{I_D} \tag{1}$$

where I_D is the PL intensity of the host and I_{DA} is the remaining PL intensity of the host in the presence of the guest. Here, γ_{ET} was calculated as 0.8 that are among the best reported in CDs based active layers applied to LECs.[15,17,47] Finally, in order to deepen the understanding of BN-CDs PL behavior from solution to solid-state, we carried out excitation-emission scans covering the whole visible range at different stage of the devices fabrication – see Experimental Section for further details. More in detail, as shown in **Figure 6**, upon addition of the electrolyte components both solution and thin-films exhibit a strong excitation-dependent PL response covering the whole visible range and the relative intensity of the lower emissive species is enhanced upon film formation. At this point, it is possible to asset that BN-CDs undergo ions-induced aggregation already in solution and the presence of lower energy emissive aggregates is promoted upon film formation. Similar findings have been already reported.[16,47,53]

2.3. Electrochemical Behavior of BN-CDs

At first, the electrochemical properties of BN-CDs were studied via cyclic voltammetry (CV) and square wave voltammetry (SWV) assays in phosphate-buffered saline (PBS) water solutions at different scan rates (Figure S11, Supporting Information). The electrochemical behavior is characterized by a *quasi*-reversible reduction peak at −0.60 V (peak potential vs. Ag/AgCl). No other redox processes were noted in this potential window. This is in line with the high optical bandgap (i.e., 3.13 eV) that would require a broad electrochemical window. Thus, we focused on studying the electrochemical behavior of the above thin-films optimized for LECs. In detail, a thin active layer (90 nm) that consists of SPPO13:THABF$_4$:BN-CD:TMPE in 1:0.2:0.6:0.2 mass ratio was spin-coated on glass/Indium Tin Oxide (ITO) /poly(3,4-ethylenedioxythiophene):polystyrene sulfonate (PEDOT:PSS) as anode and finalized by depositing via physical vapor deposition aluminum as cathode – see experimental section for further details. Electrochemical impedance spectroscopy (EIS) assays was performed to investigate ionic and electrical conductivities.[2,54] The EIS data were analyzed using a single resistor/capacitor equivalent circuit model (Figure S12 and Table S5, Supporting Information), enabling to study the formation of

© 2024 The Author(s). Advanced Optical Materials published by Wiley-VCH GmbH

21951071, 2024, 27, Downloaded from https://advanced.onlinelibrary.wiley.com/doi/10.1002/adom.202400618 by Universita Di Torino, Wiley Online Library on [13/03/2025]. See the Terms and Conditions (https://onlinelibrary.wiley.com/terms-and-conditions) on Wiley Online Library for rules of use; OA articles are governed by the applicable Creative Commons License

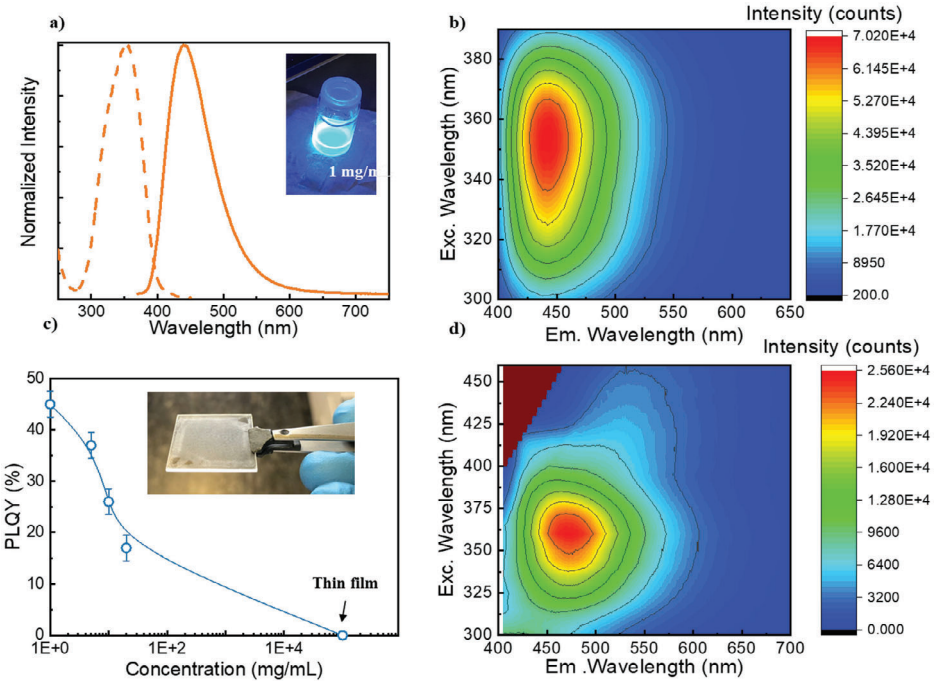

Figure 5. a) Normalized excitation (dashed line) and emission (solid line) spectra of BN-CDs in aqueous solution. The inset depicts a photograph of the solution at 1 mg mL^{-1} under UV lamp (305 nm). b) 2D-plot of PL intensity of 1 mg mL^{-1} solution as a function of both excitation and emission wavelength. c) The PLQY values as a function of BN-CD concentration in aqueous solution as well as in spin-coated thin-films. The inset displays a photograph of the spin-coated film on a glass substrate. d) 2D-plot of PL intensity of 20 mg mL^{-1} solution as a function of both excitation and emission wavelength.

electrochemical double layers (EDLs) and electrochemical doping that simultaneously occur upon increasing the applied voltage from 0 to 5 V. In short, the Nyquist plots show a similar pattern consisting of one semicircle, from which the resistance (R_{lec}) can be attributed to the dynamics of EDLs at applied voltages below the energy bandgap of the emitter ($V_{inj} < E_{gap}$) and the reduction of the non-doped region upon charge injection ($V_{inj} > E_{gap}$).[55] In line with the literature, BN-CDs-based LECs exhibited a typical LEC behavior with a R_{lec} profile related to *i)* an initial exponential decrease at biases below theenergy gap of the emitter (<3.1 V) that corresponds to the formation of EDLs at the electrode interface and *ii)* a plateau attributed to the formation of doped regions and the auto-sustained growth of doped regions and charge recombination at the intrinsic region (Figure S12, Supporting Information).

2.4. White Electroluminescent Behavior of BN-CDs LECs

After demonstrating the LEC behavior of the BN-CDs-based active layer, the devices were driven at pulsed current scheme based on a block wave at 1000 Hz and duty cycle of 50% at 200 mA cm^{-2} current compliance that has led to best LECs performances regarding stability and turn-on times.[11,56,57] **Figure 7a** shows the average voltage and luminance for LECs that follow the typical behavior of ionic-based lighting devices.[15,58] In particular, the average voltage exponentially decrease down to 5 V from its initially high voltage (≈7 V) due to the EDLs formation. This goes hand-in-hand with the increase of the luminance that reaches its maximum value at 40 cd m^{-2} and quickly reduces leading to a lifetime (time to reach half of the maximum luminance) of ≈1.3 h. This represents an order of magnitude improvement with respect to the prior-art carbon-based CDs-LECs – Table S1 (Supporting Information).[15,17] The relatively slow reduction in brightness must be related to the shrink of the emissive non-doped region due the imbalanced n-/p-doped growing zones, since the average voltage holds fairly stable, inferring a low electrochemical degradation of the active layer.[15,27] The moderate level of luminance reached corresponds to max current efficacy, external quantum efficiency, and luminous efficiency of 0.04 cd A^{-1}, 0.038%, and 0.046 lm W^{-1}, respectively.

Much more relevant is the analysis of the device chromaticity over time. In stark contrast with the blue PL features, these devices exhibited a white EL response covering the entire visible range (Figure 7b). Specifically, the EL spectrum consists of a broad peak (FWHM = 160 nm) centered at 520 nm flanked by a shoulder located at 430 nm that led to a daylight white emission with x/y CIE coordinates of 0.30/0.35, CCT of 6795 K, and CRI of 87. The EL spectra are mainly related to the lower energy emissive species promoted upon aggregation – vide supra and Figure 7c.

Table 1. Photophysical properties of SPPO13:THABF$_4$:BN-CD:TMPE thin films.

Composition	λ_{em} [nm]	<τ> [ns]	PLQY [%]	k_{rad} [x10^7 s^{-1}]
1:0.2:0.0:0.0	365	4.15	13	3.1
1:0.2:0.0:0.2	365	5.0	14	2.9
1:0.2:0.6:0.2	365, 440	1.69	15	8.9

© 2024 The Author(s). Advanced Optical Materials published by Wiley-VCH GmbH

21951071, 2024, 27, Downloaded from https://advanced.onlinelibrary.wiley.com/doi/10.1002/adom.202400618 by Universita Di Torino, Wiley Online Library on [13/03/2025]. See the Terms and Conditions (https://onlinelibrary.wiley.com/terms-and-conditions) on Wiley Online Library for rules of use; OA articles are governed by the applicable Creative Commons License

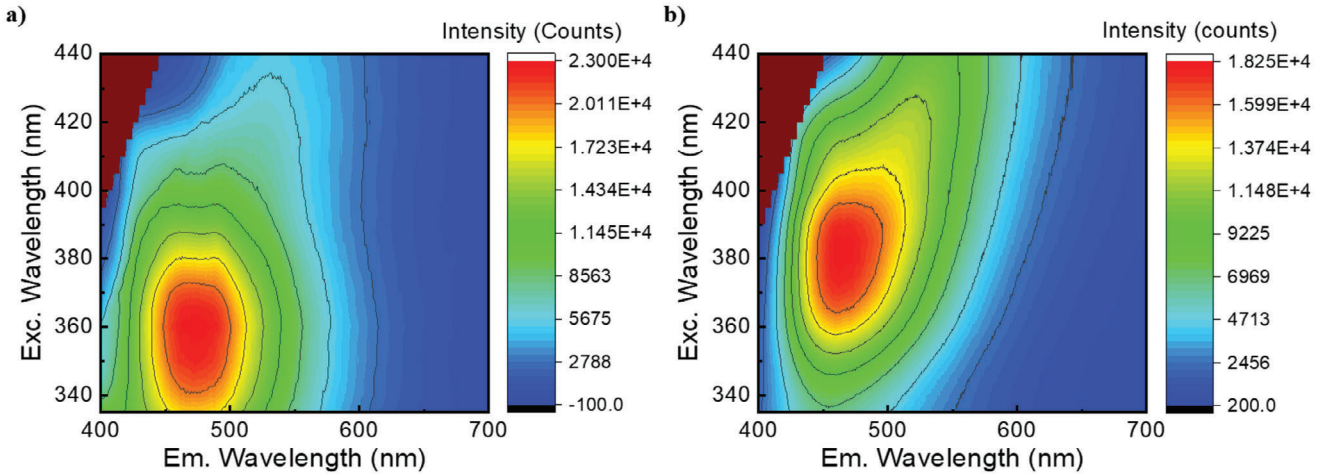

Figure 6. Excitation-dependent PL response of BN-CDs:electrolyte in solution- (a) and solid-state (b).

Unfortunately, the shape of the EL spectrum changes until the maximum luminance is reached, showing a gradual red-shift (up to 554 nm) that results in a final warm/yellowish white color associated to x/y CIE coordinates of 0.35/0.39.

Based on the prior art of CDs and white LECs,[1,15,17,58,59] three hypotheses can be postulated regarding the gradual red-shift that occurs *in operando*: *i)* thermal/photo-activated emission processes, *ii)* electric field-dependent chromaticity, and *iii)* microcavity effects due to the dynamic changes of the *p–i-n* junctions, as suggested by the luminance profile.[58,60] The earlier was studied in BN-CDs-based coatings under UV excitation (380 nm; 0.62 W) at 50 °C as noted in LECs *in operando* monitoring the PL response over time (Figure S13, Supporting Information; see experimental section for further details).[61,62] The expected intense blue PL response was measured, noting a decrease in intensity of overtime without any new emission bands evolving. Thus, we can exclude the presence of photo-/thermal-induced low-energy emitting degradative species. The second was investigated by performing a series of luminance-current-voltage (L-I-V) scans in the 0–15 V range with a scan rate of 100 mV s^{-1} to gradually increase the applied electric field (Figure S14, Supporting Information). Upon repetitive scans, the EL spectrum consists of a whitish broad emission band that gradually increases in intensity with the applied voltage and holds constant over scans. Thus, we can discard the impact of electric field variation on electroluminescent emission features and/or the formation of low-energy emitting species. Consequently, we can conclude that the red-shift *in operando* of the EL spectrum is related to a microcavity effects related to changes of the position of the emissive (*i*) zone. Similar systems have already reported this effect.[56,58,63]

Finally, our findings are, therefore, suggesting that the interaction with the electrolyte and the BN-CDs, and the control of the position of the emissive zone are key to tune device's chromaticity. Thus, a better design of the host matrix joint to a surface functionalization of CDs will be paramount to further enhance the performance of BN-CDs-based white LECs.

3. Conclusion

This work discloses *i*) a cost-effective and easily scalable water-based microwave-assisted synthesis procedure of homogenous BN-CDs and *ii*) a rationale of the origin of the blue PL and white EL responses of B- and N-doped CDs, achieving white

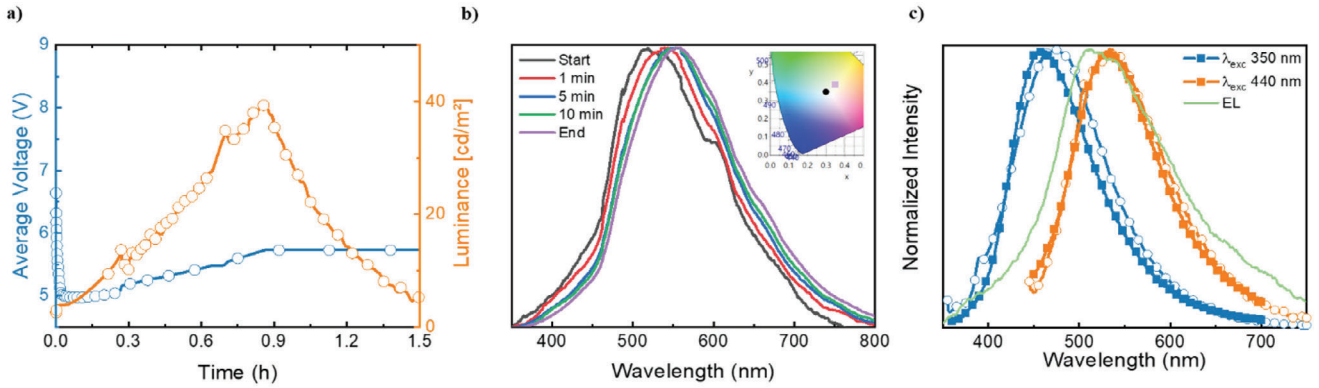

Figure 7. a) Average voltage profiles and luminance of LECs driven at pulsed current density of 200 mA cm^{-2}. b) Temporal changes of the EL spectrum (see legend) and x/y CIE color coordinates (inset – right; the starting color is depicted by the black circle and the final color by the violet square) of BN-CDs-based LECs. c) Normalized emission intensity of BN-CDs:electrolyte in solution- (empty circles) and solid-state (filled squares) at excitation wavelength of 350 nm (blue) and 440 nm (orange). The EL spectrum is depicted in green.

© 2024 The Author(s). Advanced Optical Materials published by Wiley-VCH GmbH

21951071, 2024, 27, Downloaded from https://advanced.onlinelibrary.wiley.com/doi/10.1002/adom.202400618 by Universita Di Torino, Wiley Online Library on [13/03/2025]. See the Terms and Conditions (https://onlinelibrary.wiley.com/terms-and-conditions) on Wiley Online Library for rules of use; OA articles are governed by the applicable Creative Commons License

LECs with superior stabilities compared to the prior-art CD-based LECs.[15,17,27] In short, a comprehensive microscopic and spectroscopic study (AFM, TEM, XPS, Raman, and UV–vis/emission) confirmed that the BN-CDs feature an amorphous carbon-core doped with B (0.14%) and N (5.1%) and a bright (PLQY = 42%; τ = 6.77 ns), narrow (60 nm), and excitation-independent blue (440 nm) emission in solution that is attributed to n−p* surface states. Moreover, we circumvented the common aggregation-induced emission quenching of the BN-CDs in thin-films combining a hydrophilic host and ion electrolyte. This resulted in an excitation-dependent emission that covers the whole visible range. Capitalizing on this, we fabricated the first white LECs with remarkable stabilities (lifetime) compared to the prior-art. More importantly, we highlighted that the complex interplay between the ion electrolyte and the n–π^* surface states of the BN-CDs is key to control device chromaticity and performance in the near future. Overall, this work embraces the principles of green optoelectronics by employing cost-effective and abundant emitters, conducting water-based synthesis under mild conditions, and utilizing low-toxicity solvents for the fabrication of devices that has reached interesting lighting features.

4. Experimental Section

Synthesis of B, N-Doped Carbon Dots: Citric acid (monohydrate, ≥98%), boric acid (ACS reagent, ≥99.5%), and urea (ACS reagent, 99.0-100.5%) were purchased from Sigma-Aldrich. MilliQ water was produced by Millipore MilliQ Plus 185 (Waters) purifying system. The cellulose ester ready-to-use dialysis devices Float-A-LyzerG2 were purchased from Spectra/Por Repligen Corporation (USA). The TEM grids (LC300-CU Lacey Carbon Film, Copper, 300 mesh) were purchased from Electron Microscopy Sciences. The AFM Mica substrates (PELCO Mica Sheet) and specimen disks (d = 12 mm) were purchased from TED Pella Inc., while HQ:NSC19/AL_BS cantilevers from MikroMash Innovative Solutions were used.

For the synthesis, 4 mL of aqueous solution of citric acid, boric acid, and urea (1:1:1 mass ratio, C = 0.15 g mL^{-1}) was placed in a 10-mL glass vial and kept for 4 min under microwave irradiation and high stirring rate at 190 °C and 240 psi using a Discover SP Microwave (ActiVent, CEM Corporation). The synthesis was controlled by Synergy software. The as-prepared dark emerald-green solution of BNC nanodots was purified by dialysis for 48 h against MilliQ water using a cellulose ester ready-to-use dialysis device with molecular weight cut-off of 100–500 Da. The purified solution of BN-CDs was lyophilized for 3 days in a freeze-dryer chamber (ScanVac Coolsafe, Labogene). The 123 mg of dark emerald-green powder was obtained with 20% yield.

Characterization of B, N-Doped Carbon Dots: TEM imaging was carried out using an EM 208 microscope (Philips) equipped with a Quemesa camera (Olympus Soft Imaging Solutions). The images were acquired at a voltage of 100 kV using RADIUS software, while the size measurements were performed using ImageJ software. The AFM analysis of pristine BN-CDs was performed using a Multimode Scanning Probe Microscope (Veeco) equipped with a Nanoscope Controller. The images were acquired using n-type silicon AFM cantilevers (HQ:NSC19/AL_BS, µmasch) at room temperature in air. The AFM data analysis was performed using Gwyddion software. ^{1}H-NMR spectroscopy was performed using Varian 400 MHz and DMSO-d_6 as a solvent. The ATR-FTIR spectroscopy was performed using the IRAffinity-1S (Shimadzu) spectrometer and germanium (Ge) prism.

To perform XPS, Raman spectroscopy, and XRD analysis, BN-CDs diluted in ethanol were deposited onto a Cu round-shaped sample holder of 8 mm diameter.

The XPS measurements were performed in a SPECS Phoibos system equipped with an XRM50 X-ray source set to Al Kα (1486.7 eV) used along with a monochromator to excite the sample with a beam spot of 0.4 mm diameter at 55° incidence. The acceleration voltage was set to 11 kV and a power of 250 W was used for all measurements. The HAS 3500 hemispherical analyzer with a pass energy of 50 eV was employed to analyze the photoemission.

All XPS data were analyzed using CASA XPS. Shirley and Tougaard backgrounds were subtracted from the different binding energy regions of the elements. All XPS spectra have been calibrated relative to the Cu2p peak. For atomic concentrations' calculations, the peak areas were corrected for their relative sensitivity factors.[64,65]

The Raman spectroscopy characterization was performed using an inverted confocal Raman microscope (LabRam HR, Horiba Jobin Yvon) with a 50x objective and grating of 1800 lines mm^{-1}. A He/Ne laser (633 nm) was used to filter the backscattered light, which was subsequently directed to the spectrograph and to the CCD detector; further details of the setup can be found in the following refs. [66,67]. The XRD measurements were performed with a Philips PANanalytical SR5161 X'Pert XRD system with 40 kV and 30 mA.

The UV–vis spectra in solution were recorded using a UV–vis–NIR Cary 5000 Varian (Agilent Technologies) spectrophotometer and quartz cuvette with a 10-mm light path. The PL spectra in solution were acquired on an FS5 Spectrofluorometer (Edinburgh Instruments Ltd.) using Fluoracle software. The absolute quantum yield (QY) measurements were performed using an integrating sphere and MilliQ-water as a reference. Both UV–vis and PL spectra in solution were recorded in MilliQ water. For the solvent/ions interaction experiment 20 µL of TMPE in cyclohexanone (100 mg mL^{-1}) and 20 µL of $THABF_4$ in cyclohexanone (20 mg mL^{-1}) were added to 2 mL of BN-CDs in ethanol 80% (1 mg/mL). The same solution has been drop-casted on a quartz slide for the solid-state experiment.

For thin-film preparation via spin coating, SPPO13 was dissolved in cyclohexanone at 10 mg mL^{-1} upon heating at 50 °C for 2 h, while BN-CDs were dispersed in ethanol 80% at 8 mg mL^{-1}. Cyclohexanone was selected as solvent due to its high green score[68] while ensuring layer orthogonality with the underlying layer of PEDOT:PSS in the device architecture. The final layer composition was SPPO13:$THABF_4$:BN-CDs:TMPE in a mass ratio of 1:0.2:0.6:0.2. The solutions were spin-coated on quartz slides at 2000 rpm for 30 s leading to homogeneous films. The morphology of the obtained BN-CDs films was monitored via atomic force microscopy (MFP-3D Origin+, Asylum Research) in a 100 µm^2 area, and further analyzed with Gwyddion software. The PL spectra and PLQY values were measured with an FS5 Spectrofluorometer with integrating sphere SC-30 (Edinburgh Instruments). The excited-state lifetimes were acquired with a TC-SPC diode at λ = 377.6 nm. For solid-state photobleaching tests, rubber-like coatings were prepared with a mass ratio of 4:1 TMPE:PEO (TMPE; $M_n \approx 450$ and PEO; $M_v \approx 5 \times 10^6$). To carry out the photostability and conversion measurements the coatings were placed directly on the unmodified commercial LED. The EL spectra were recorded with an Avantes Spectrometer 2048L (300 VA grating, 200 µm slit, CCD detector) coupled with an AvaSphere 30-Irrad Integrated sphere, monitoring the temperature using a thermographic camera (FLIR ETS320). The employed power source was a Keithley 2231-A-30-3.

Cyclic voltammetry measurements were carried out in a cylindrical one-compartment cell with a three-electrode set-up. A platinum disk working electrode with a diameter of 3.0 mm, a Pt wire as counter electrode, and Ag/AgCl wire as reference electrode were used. Prior to every measurement, the working electrode was polished with alumina slurry 0.04 mm from Schmitz Metallographie GmbH. The potential was controlled by a Metrohm µAutolabIII potentiostat. All measurements were conducted in PBS buffer solution.

Device Fabrication and Characterization: ITO substrates were purchased from Naranjo Substrates with an ITO thickness of 130 nm. They were extensively cleaned using detergent, water, ethanol, and propan-2-ol as solvents in an ultrasonic bath (frequency 37–70 Hz) for 15 min each. Afterward, the slides were dried with inert gas and put in a UV–ozone cleaner for 8 min. The clean plates were coated with 70-nm PEDOT:PSS layers via spin coating to increase the device reproducibility. To this end, an aqueous solution of PEDOT:PSS was filtered and mixed with propan-2-ol in a ratio of 3:1. From this solution, 50 µL were dropped onto the substrate at a rotation speed of 2000 rpm and spun for 60 s.

© 2024 The Author(s). Advanced Optical Materials published by Wiley-VCH GmbH

21951071, 2024, 27, Downloaded from https://advanced.onlinelibrary.wiley.com/doi/10.1002/adom.202400618 by Universita Di Torino, Wiley Online Library on [13/03/2025]. See the Terms and Conditions (https://onlinelibrary.wiley.com/terms-and-conditions) on Wiley Online Library for rules of use; OA articles are governed by the applicable Creative Commons License

The resulting layers were dried on a hotplate at 120 °C and stored under N_2. The active layers were deposited from blend solutions and spin coated at 800 rpm for 30 s, at 1500 rpm for 30 s, and at 3000 rpm for an additional 10 s, resulting in an 80–100 nm thick film. For functional LECs fabrication, glass/ITO/PEDOT:PSS substrates were used and after the deposition of the active layer the devices were dried under vacuum for 2 h and transferred to an inert-atmosphere glovebox. Finally, the aluminum cathode (90 nm) was thermally evaporated onto the active layer using a shadow mask under high vacuum ($<10^{-6}$ mbar) in an Angstrom Covap evaporator integrated into the inert-atmosphere glovebox. Time dependence of luminance, voltage, and current was measured by applying constant and/or pulsed voltage and current by monitoring the desired parameters simultaneously using an Avantes spectrophotometer (Avaspec-ULS2048L-USB2) in conjunction with a calibrated integrated sphere Avasphere 30-Irrad and Botest OLT OLED Lifetime-Test System. EL spectra were recorded using the above-mentioned spectrophotometer. EIS assays were carried out with a potentiostat/galvanostat (Metrohm µAutolabIII) equipped with a frequency response analyzer module (FRA2). Measurements were performed at the applied voltage range from 0 to 5 V and fitted with the Nova 2.1 software using the circuit model shown in Figure S7 (Supporting Information). R_{LEC} represents the effective resistance of the active layer, including injection resistances, CPE_{LEC} represents the capacitance of the two electrodes contacting the film. The second resistor (R_{series}) represents all external resistances, including those of the ITO and Al electrodes. The AC signal amplitude was set to 10 mV, modulated in a frequency range from 10^1 to 10^6 MHz.

Statistical Analysis: Thin films statistics involve three replicates for each composition, while the device statistics involve up to five different devices, i.e., a total number of 20 pixels. The absence of outliers has been confirmed via t-test. The software OriginPro 2020 has been used for data analysis and evaluation.

Supporting Information

Supporting Information is available from the Wiley Online Library or from the author.

Acknowledgements

L.M.C., V.K., and S.C.J. contributed equally to this work. L.M.C., S. C., R.D.C., V.K., T.D.R., S.C.J., and I.M.N.G. acknowledge the European Union's Horizon 2020 Program under grant agreement MSCA-ITN STiBNite No. 956923. S.F. and R.D.C. acknowledge the European Union's innovation FET-OPEN under grant agreement ARTIBLED No. 863170.

Open access funding enabled and organized by Projekt DEAL.

Conflict of Interest

The authors declare no conflict of interest.

Data Availability Statement

The data that support the findings of this study are available from the corresponding author upon reasonable request.

Keywords

boron and nitrogen carbon nanoparticles, green emitters, light-emitting electrochemical cells, water-based microwave-assisted synthesis, white electroluminescence

Received: April 23, 2024
Revised: May 30, 2024
Published online: June 21, 2024

[1] E. Fresta, R. D. Costa, *Adv. Funct. Mater.* **2020**, *30*, 1908176.
[2] L. D. Bastatas, K. Y. Lin, M. D. Moore, K. J. Suhr, M. H. Bowler, Y. Shen, B. J. Holliday, J. D. Slinker, *Langmuir* **2016**, *32*, 9468.
[3] J. Xu, A. Sandström, E. M. Lindh, W. Yang, S. Tang, L. Edman, *ACS Appl. Mater. Interfaces* **2018**, *10*, 33380.
[4] A. Sandström, A. Asadpoordarvish, J. Enevold, L. Edman, *Adv. Mater.* **2014**, *26*, 4975.
[5] E. Auroux, A. Sandström, C. Larsen, P. Lundberg, T. Wågberg, L. Edman, *Org. Electron.* **2020**, *84*, 105812.
[6] J. D. Slinker, A. A. Gorodetsky, M. S. Lowry, J. Wang, S. Parker, R. Rohl, S. Bernhard, G. G. Malliaras, *J. Am. Chem. Soc.* **2004**, *126*, 2763.
[7] P. Lundberg, Y. Tsuchiya, E. M. Lindh, S. Tang, C. Adachi, L. Edman, *Nat. Commun.* **2019**, *10*, 5307.
[8] E. Nannen, J. Frohleiks, S. Gellner, *Adv. Funct. Mater.* **2020**, *30*, 1907349.
[9] A. Mishra, R. Bose, Y. Zheng, W. Xu, R. McMullen, A. B. Mehta, M. J. Kim, J. W. P. Hsu, A. V. Malko, J. D. Slinker, *Adv. Mater.* **2022**, *34*, 2203226.
[10] S. Lipinski, L. M. Cavinato, T. Pickl, G. Biffi, A. Pöthig, P. B. Coto, J. Fernández-Cestau, R. D. Costa, *Adv. Opt. Mater.* **2023**, *11*, 2203145.
[11] L. M. Cavinato, K. Yamaoka, S. Lipinski, V. Calvi, D. Wehenkel, R. van Rijn, K. Albrecht, R. D. Costa, *Adv. Funct. Mater.* **2023**, *33*, 2302483.
[12] L. M. Cavinato, G. Millán, J. Fernández-Cestau, E. Fresta, E. Lalinde, J. R. Berenguer, R. D. Costa, *Adv. Funct. Mater.* **2022**, *32*, 2201975.
[13] T. Hu, Z. Wen, C. Wang, T. Thomas, C. Wang, Q. Song, M. Yang, *Nanoscale Adv* **2019**, *1*, 1413.
[14] Y. Zhang, P. Zhuo, H. Yin, Y. Fan, J. Zhang, X. Liu, Z. Chen, *ACS Appl. Mater. Interfaces* **2019**, *11*, 24395.
[15] Y. Liu, S. Tang, X. Wu, N. Boulanger, E. Gracia-Espino, T. Wågberg, L. Edman, J. Wang, *Nano Res.* **2022**, *15*, 5610.
[16] G. Minervini, A. Madonia, A. Panniello, E. Fanizza, M. L. Curri, M. Striccoli, *Nanomaterials* **2023**, *13*, 374.
[17] S. Tang, Y. Liu, H. Opoku, M. Gregorsson, P. Zhang, E. Auroux, D. Dang, A.-V. Mudring, T. Wågberg, L. Edman, J. Wang, *Green Chem.* **2023**, *25*, 9884.
[18] H. Hu, B. Tang, H. Wan, H. Sun, S. Zhou, J. Dai, C. Chen, S. Liu, L. J. Guo, *Nano Energy* **2020**, *69*, 104427.
[19] H. He, X. Wang, Z. Feng, T. Cheng, X. Sun, Y. Sun, Y. Xia, S. Wang, J. Wang, X. Zhang, *J. Mater. Chem. B* **2015**, *3*, 4786.
[20] T. V. de Medeiros, J. Manioudakis, F. Noun, J.-R. Macairan, F. Victoria, R. Naccache, *J. Mater. Chem. C* **2019**, *7*, 7175.
[21] G. Renno, F. Cardano, G. Volpi, C. Barolo, G. Viscardi, A. Fin, *Molecules* **2022**, *27*, 3856.
[22] M. Giordano, G. Volpi, C. Garino, F. Cardano, C. Barolo, G. Viscardi, A. Fin, *Dyes Pigments* **2023**, *218*, 111482.
[23] L. M. Cavinato, G. Volpi, E. Fresta, C. Garino, A. Fin, C. Barolo, *Chemistry* **2021**, *3*, 714.
[24] E. Palmieri, L. Maiolo, I. Lucarini, A. D. Fattorini, E. Tamburri, S. Orlanducci, R. Calarco, F. Maita, *Adv. Mater. Technol.* **2024**, *9*, 2301282.
[25] Q. Hong, X.-Y. Wang, Y.-T. Gao, J. Lv, B.-B. Chen, D.-W. Li, R.-C. Qian, *Chem. Mater.* **2022**, *34*, 998.
[26] B. Wang, S. Lu, *Matter* **2022**, *5*, 110.
[27] J. R. Adsetts, Z. Whitworth, K. Chu, L. Yang, C. Zhang, Z. Ding, *ChemElectroChem* **2022**, *9*, 202101512.
[28] H. Yang, Y. Liu, Z. Guo, B. Lei, J. Zhuang, X. Zhang, Z. Liu, C. Hu, *Nat. Commun.* **2019**, *10*, 1789.
[29] Y. Chen, M. Zheng, Y. Xiao, H. Dong, H. Zhang, J. Zhuang, H. Hu, B. Lei, Y. Liu, *Adv. Mater.* **2016**, *28*, 312.
[30] Z. Peng, Y. Zhou, C. Ji, J. Pardo, K. J. Mintz, R. R. Pandey, C. C. Chusuei, R. M. Graham, G. Yan, R. M. Leblanc, *Nanomaterials* **2020**, *10*, 1560.

© 2024 The Author(s). Advanced Optical Materials published by Wiley-VCH GmbH

21951071, 2024, 27, Downloaded from https://advanced.onlinelibrary.wiley.com/doi/10.1002/adom.202400618 by Universita Di Torino, Wiley Online Library on [13/03/2025]. See the Terms and Conditions (https://onlinelibrary.wiley.com/terms-and-conditions) on Wiley Online Library for rules of use; OA articles are governed by the applicable Creative Commons License

[31] G. Minervini, A. Panniello, A. Madonia, C. M. Carbonaro, F. Mocci, T. Sibillano, C. Giannini, R. Comparelli, C. Ingrosso, N. Depalo, E. Fanizza, M. L. Curri, M. Striccoli, *Carbon* **2022**, *198*, 230.
[32] F. Mocci, C. Olla, A. Cappai, R. Corpino, P. C. Ricci, D. Chiriu, M. Salis, C. M. Carbonaro, *Materials* **2021**, *14*, 770.
[33] V. Strauss, H. Wang, S. Delacroix, M. Ledendecker, P. Wessig, *Chem. Sci.* **2020**, *11*, 8256.
[34] W. Kasprzyk, T. Świergosz, S. Bednarz, K. Walas, N. V. Bashmakova, D. Bogdał, *Nanoscale* **2018**, *10*, 13889.
[35] M. Jia, L. Peng, M. Yang, H. Wei, M. Zhang, Y. Wang, *Carbon* **2021**, *182*, 42.
[36] E. Budak, C. Ünlü, *Opt. Mater.* **2021**, *111*, 110577.
[37] W. Wang, B. Wang, H. Embrechts, C. Damm, A. Cadranel, V. Strauss, M. Distaso, V. Hinterberger, D. M. Guldi, W. Peukert, *RSC Adv.* **2017**, *7*, 24771.
[38] B. Bartolomei, A. Bogo, F. Amato, G. Ragazzon, M. Prato, *Angew. Chem., Int. Ed.* **2022**, *61*, 202200038.
[39] P. N. Thang, L. X. Hung, D. N. Thuan, N. H. Yen, N. T. T. Hien, V. T. H. Hanh, N. C. Khang, J. Laverdant, P. T. Nga, *J. Mater. Sci.* **2021**, *56*, 4979.
[40] H. Wang, Q. Mu, K. Wang, R. A. Revia, C. Yen, X. Gu, B. Tian, J. Liu, M. Zhang, *Appl. Mater. Today* **2019**, *14*, 108.
[41] B. Tian, T. Fu, Y. Wan, Y. Ma, Y. Wang, Z. Feng, Z. Jiang, *J. Nanobiotechnol.* **2021**, *19*, 456.
[42] E. Budak, S. Aykut, M. E. Paşaoğlu, C. Ünlü, *Mater. Today Commun.* **2020**, *24*, 100975.
[43] S. N. Faisal, E. Haque, N. Noorbehesht, W. Zhang, A. T. Harris, T. L. Church, A. I. Minett, *RSC Adv.* **2017**, *7*, 17950.
[44] Z. Liu, Z. Mo, N. Liu, R. Guo, X. Niu, P. Zhao, X. Yang, *J. Photochem. Photobiol. Chem.* **2020**, *389*, 112255.
[45] H. K. Sadhanala, K. K. Nanda, *J. Phys. Chem. C* **2015**, *119*, 13138.
[46] C. Park, G. Shim, N. Balaji, J. Park, J. Yi, *Energies* **2020**, *13*, 3057.
[47] A. Sharma, T. Gadly, A. Gupta, A. Ballal, S. K. Ghosh, M. Kumbhakar, *J. Phys. Chem. Lett.* **2016**, *7*, 3695.
[48] X. Li, S. Zhang, S. A. Kulinich, Y. Liu, H. Zeng, *Sci. Rep.* **2014**, *4*, 4976.
[49] F. Rigodanza, M. Burian, F. Arcudi, L. Đorđević, H. Amenitsch, M. Prato, *Nat. Commun.* **2021**, *12*, 2640.
[50] M. Cacioppo, T. Scharl, L. Đorđević, A. Cadranel, F. Arcudi, D. M. Guldi, M. Prato, *Angew. Chem., Int. Ed.* **2020**, *59*, 12779.
[51] G. Sych, M. Guzauskas, D. Volyniuk, J. Simokaitiene, H. Starykov, *J. Adv. Res.* **2020**, *24*, 379.
[52] B. Stender, S. F. Völker, C. Lambert, J. Pflaum, *Adv. Mater.* **2013**, *25*, 2943.
[53] A. Terracina, A. Armano, M. Meloni, A. Panniello, G. Minervini, A. Madonia, M. Cannas, M. Striccoli, L. Malfatti, F. Messina, *ACS Appl. Mater. Interfaces* **2022**, *14*, 36038.
[54] L. D. Bastatas, M. D. Moore, J. D. Slinker, *ChemPlusChem* **2018**, *83*, 266.
[55] S. van Reenen, M. Kemerink, *Light-Emitting Electrochemical Cells*, Springer International Publishing, Cham **2017**, pp. 3.
[56] J. Ràfols-Ribé, X. Zhang, C. Larsen, P. Lundberg, E. M. Lindh, C. T. Mai, J. Mindemark, E. Gracia-Espino, L. Edman, *Adv. Mater.* **2022**, *34*, 2107849.
[57] S. Tang, P. Lundberg, Y. Tsuchiya, J. Ràfols-Ribé, Y. Liu, J. Wang, C. Adachi, L. Edman, *Adv. Funct. Mater.* **2022**, *32*, 2205967.
[58] E. Fresta, J. Dosso, J. Cabanillas-González, D. Bonifazi, R. D. Costa, *Adv. Funct. Mater.* **2020**, *30*, 1906830.
[59] M. D. Weber, J. E. Wittmann, A. Burger, O. B. Malcıoğlu, J. Segarra-Martí, A. Hirsch, P. B. Coto, M. Bockstedte, R. D. Costa, *Adv. Funct. Mater.* **2016**, *26*, 6737.
[60] E. Fresta, K. Baumgärtner, J. Cabanillas-Gonzalez, M. Mastalerz, R. D. Costa, *Nanoscale Horiz.* **2020**, *5*, 473.
[61] S. Ferrara, S. H. Mejias, M. Liutkus, G. Renno, F. Stella, I. Kociolek, J. P. Fuenzalida-Werner, C. Barolo, P. B. Coto, A. L. Cortajarena, R. D. Costa, *Adv. Funct. Mater.* **2022**, *32*, 2111381.
[62] J. Ràfols-Ribé, N. D. Robinson, C. Larsen, S. Tang, M. Top, A. Sandström, L. Edman, *Adv. Funct. Mater.* **2020**, *30*, 1908649.
[63] S. Jenatsch, M. Regnat, R. Hany, M. Diethelm, F. Nüesch, B. Ruhstaller, *ACS Photonics* **2018**, *5*, 1591.
[64] M. C. Biesinger, *Surf. Interface Anal.* **2017**, *49*, 1325.
[65] A. C. Miller, G. W. Simmons, *Surf. Sci. Spectra* **1993**, *2*, 55.
[66] S. C. S. Lai, S. E. F. Kleyn, V. Rosca, M. T. M. Koper, *J. Phys. Chem. C* **2008**, *112*, 19080.
[67] O. Diaz-Morales, F. Calle-Vallejo, C. de Munck, M. T. M. Koper, *Chem. Sci.* **2013**, *4*, 2334.
[68] C. Larsen, P. Lundberg, S. Tang, J. Ràfols-Ribé, A. Sandström, E. Mattias Lindh, J. Wang, L. Edman, *Nat. Commun.* **2021**, *12*, 4510.

© 2024 The Author(s). Advanced Optical Materials published by Wiley-VCH GmbH

21951071, 2024, 27, Downloaded from https://advanced.onlinelibrary.wiley.com/doi/10.1002/adom.202400618 by Universita Di Torino, Wiley Online Library on [13/03/2025]. See the Terms and Conditions (https://onlinelibrary.wiley.com/terms-and-conditions) on Wiley Online Library for rules of use; OA articles are governed by the applicable Creative Commons License